Qeios

Research Article

A High-Performance All-Silicon Photodetector Enabling Telecom-Wavelength Detection at Room Temperature

Mohd Saif Shaikh[1,2], Mircea-Traian Catuneanu[2], Ahmad Echresh[1], Rang Li[1,2], Shuyu Wen[1], Guillermo Godoy-Pérez[1], Slawomir Prucnal[1], Manfred Helm[1,2], Yordan M. Georgiev[1,3], Kambiz Jamshidi[2], Shengqiang Zhou[1], Yonder Berencén[1]

1. Institute of Ion Beam Physics and Materials Research, Helmholtz-Zentrum Dresden-Rossendorf, Dresden, Germany; 2. Dresden University of Technology, Germany; 3. Bulgarian Academy of Sciences, Sofia, Bulgaria

Photonic integrated circuits (PICs) are crucial for advancing optical communications, promising substantial gains in data transmission speed, bandwidth, and energy efficiency compared to conventional electronics[1]. Telecom-wavelength photodetectors, operating near 1550 nm, are indispensable in PICs, where they enable the sensitive and low-noise conversion of optical signals to electrical signals for efficient data processing. While silicon is ideal for passive optical components, its limited absorption in the optical telecommunication range (1260-1625 nm) typically necessitates integrating an alternative material, such as germanium[2], for photodetection — a process that introduces significant fabrication challenges[3]. Here, we present a high-performance, all-silicon photodetector, grating- and waveguide-coupled, which operates at room temperature within the optical telecom C band. By introducing deep-level impurities into silicon at concentrations close to the solid-solubility limit, we enable efficient sub-bandgap absorption without compromising recombination carrier lifetimes and mobilities. This detector achieves a responsivity of 0.56 A/W, a quantum efficiency of 44.8%, a bandwidth of 5.9 GHz, and a noise-equivalent power of 4.2×10^{-10} W/Hz$^{1/2}$ at 1550 nm, fulfilling requirements for telecom applications. Our approach provides a scalable and cost-effective solution for the monolithic integration of telecom-wavelength photodetectors into silicon-based PICs, advancing the development of compact photonic systems for modern communication infrastructures.

Corresponding authors: Mohd Saif Shaikh, m.shaikh@hzdr.de; Shengqiang Zhou, s.zhou@hzdr.de; Yonder Berencén, y.berencen@hzdr.de

Introduction

The escalating demands for bandwidth, speed, and energy efficiency in modern computing systems drive the adoption of optical interconnects, which offer several advantages over conventional electronic links, including lower latency, higher data transmission rates, and reduced power consumption[1]. These benefits have made photonic integrated circuits (PICs) a promising foundation for next-generation communications and data processing, where dense, efficient, and scalable optical components are essential to meet the demands of high-performance computing and AI-driven applications[4][5]. Among these components, telecom-wavelength photodetectors (PDs) are indispensable, as they convert optical signals into electrical signals for communication and data processing[6].

Silicon photonics, leveraging CMOS-compatible processes, enables the development of cost-efficient, high-density PICs that seamlessly integrate optical I/O modules with conventional electronic processors[1][7]. While silicon's transparency in all the optical telecommunication bands makes it well-suited for passive optical components like waveguides, couplers, and splitters, its bandgap (1100 nm cutoff) precludes efficient detection at telecom wavelengths. To address this demand, photodetection has traditionally relied on heteroepitaxial integration of germanium (Ge) with silicon[2], enabling responsivity at telecom wavelengths. However, Ge-based photodetectors present inherent challenges, including high dark currents, thermal sensitivity, and costly high-temperature growth processes that complicate scaling and limit compatibility with CMOS foundries.

Extensive research has sought to overcome these limitations through alternative silicon-based sub-bandgap photon detection approaches. Hyperdoping of silicon with deep-level impurities offers a path to achieve room-temperature sub-bandgap absorption for telecom wavelengths while maintaining CMOS compatibility[8]. Alternatively, techniques such as two-photon absorption (TPA), photon-assisted tunneling (PAT), the creation of dislocation loops, and optical resonant enhancement in microring resonators (MRRs) have also shown promise in enhancing responsivity and absorption efficiency at telecommunication wavelengths[9][10][11]. However, each approach faces trade-offs; for instance, TPA and PAT suffer from inherently low responsivity, dislocation loops enable only weak infrared absorption, and resonant cavities like MRRs, while enhancing absorption of TPA and PAT through resonant light trapping

and field amplification, introduce crosstalk in densely packed wavelength-division multiplexing systems and limit bandwidth due to long photon lifetimes. Additionally, hyperdoping strategies that push impurity concentrations above the solid-solubility limit result in extremely short carrier recombination lifetimes (1-200 picoseconds)[12][13] and significantly reduced carrier mobilities (10-40 cm^2/V.s)[12][14]. Although this approach enhances room-temperature photoresponse at telecommunication wavelengths[15][16], it compromises key performance metrics of the photodetector[12].

In this work, we demonstrate a scalable, high-performance solution: an all-silicon grating- and waveguide-coupled p-i-n photodetector operating at telecom wavelengths, enabled by introducing Te impurities at concentrations close to the equilibrium solid-solubility limit (3.5×10^{16} cm^{-3})[17] to create deep-level intragap states. This method allows room-temperature sub-bandgap photoresponse across all the optical telecommunication bands while avoiding the issues of high carrier recombination and low carrier mobility associated with hyperdoped silicon approaches. Operating within the optical C band, our detector achieves a responsivity of 0.56 A/W, a quantum efficiency of 44.8%, a noise-equivalent power (NEP) of 4.2×10^{-10} W/Hz$^{1/2}$, a linear dynamic range of 33.7 dB, and a calculated bandwidth of 5.9 GHz. This CMOS-compatible approach significantly simplifies fabrication, reduces costs, and supports monolithic integration within silicon photonic systems. Our results highlight the potential of Te-implanted Si photodetectors as a viable alternative to hybrid Ge-based solutions, advancing the integration of efficient, compact, and scalable photonic components.

Results

Device structure and fabrication

In a photonic-grade silicon-on-insulator (SOI) chip with a 220 nm-thick Si device layer over a 2000 nm buried silicon dioxide (BOX) layer, we designed and fabricated monolithic grating- and waveguide-coupled Si p-i-n photodetectors (GWG-PDs) with varying detector absorption lengths (L) from 300 μm to 1000 μm (Fig. 1a). Grating couplers and single-mode rib waveguides were designed and simulated using finite-difference time-domain (FDTD) method[18] to couple off-chip light from a 1550 nm single-mode fiber laser into the photodetector, which then converts the incident light into a measurable photocurrent (Fig. 1b).

Grating couplers, along with tapers, are used to couple and confine the 1550 nm light from the fiber laser into a single-mode rib waveguide, with the light incident at a 10-degree angle relative to the surface

normal of the device layer. The p–i–n detector is fabricated at the end of the single-mode rib waveguide (Fig. 1c).

The cross-section of the detector's active area (140 nm etch depth and 450 nm width) is created by implanting deep-level Te impurities at two different energies through a window, forming a 140 nm-deep region with uniform Te doping. Next, p- and n-type regions are formed by implanting B and P, respectively, through two additional windows on the chip floor, each positioned 550 nm away from the edges of the Te-implanted region (Fig. 1d). The P and B dopants were first activated using a rapid thermal annealing (RTA) process, followed by a separate RTA step with distinct parameters to activate the Te atoms. Subsequently, Ti/Au metal contacts were formed on the p- and n-doped regions. Details of the fabrication process are provided in Methods and the Supplementary Information.
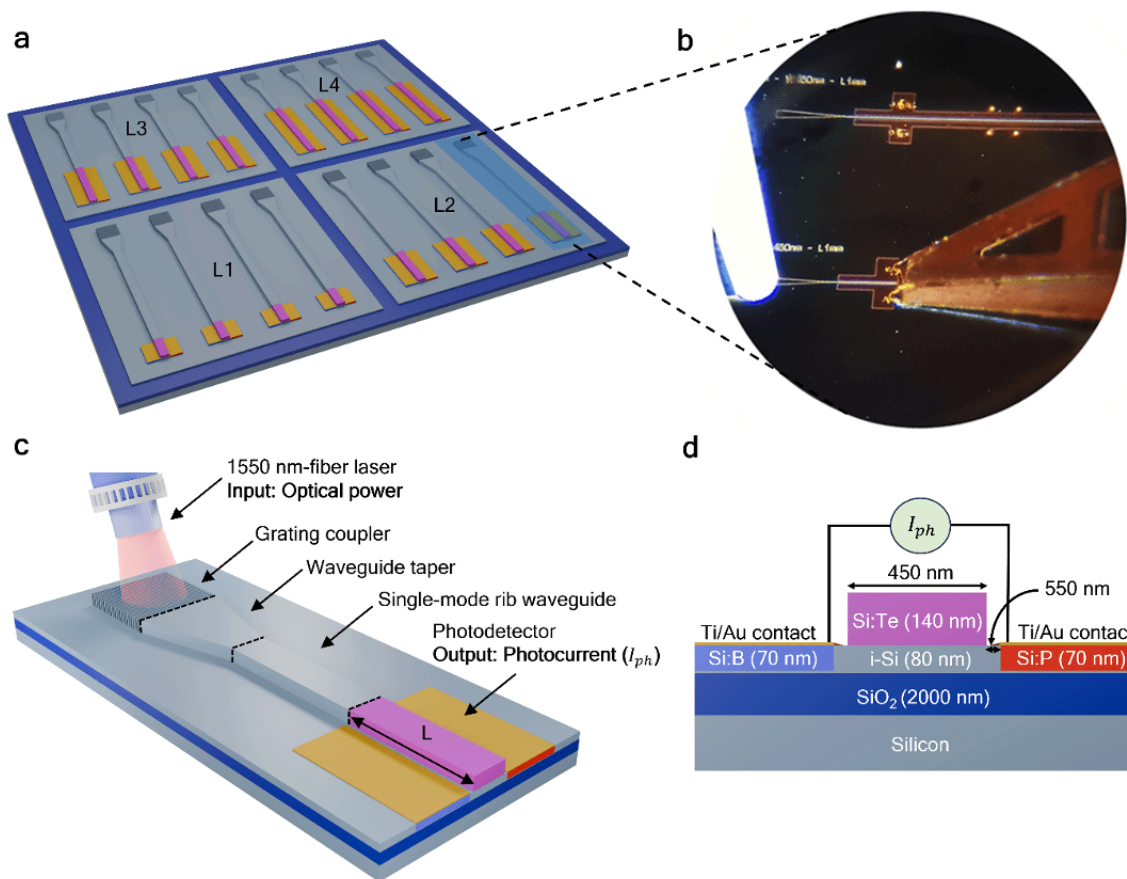
Figure 1. Design of the grating- and waveguide-coupled photodetector. a, Schematic of an SOI chip with photodetectors, each featuring different absorption region lengths (L1, L2, L3, and L4) coupled to waveguides and grating couplers. **b,** Optical microscope image of a GWG-PD, showing the 1550 nm-fiber laser (left) used to couple light through the grating coupler and detect a measurable photocurrent in the detector with electrical probes (right). **c,** Schematic of the full GWG-PD. Incident light from the 1550 nm-fiber laser is coupled into the SOI chip through a grating coupler and then confined into a single-mode rib waveguide via a waveguide taper. The waveguide is laterally coupled to the detector, where the light is detected by the p–i–n junction, producing a measurable photocurrent. **d,** Cross-sectional sketch of the p–i–n GWG-PD, illustrating the Te-implanted Si optical absorption region optimized for telecom wavelengths, integrated along the single-mode rib waveguide. Below this, the intrinsic region is sandwiched between B-doped (p-type) and P-doped (n-type) Si regions, with Ti/Au metal contacts simultaneously formed on the p- and n-doped regions. All schematics are not drawn to scale.

Device characterization

Figure 2a shows a dark current-voltage (I-V) curve for the GWG-PD at room temperature under both forward and reverse bias conditions. In reverse bias, the GWG-PD exhibits rectifying behavior, with a dark current of about 2 μA at a reverse voltage of -9 V.

Before conducting the optoelectronic characterization of the GWG-PD, we deliberately measured over 20 control passive devices that included an input grating coupler, a single-mode rib waveguide, and an output coupler. This was done to estimate the total optical loss from these structures, which must be considered when calculating responsivity. Our analysis revealed that the average optical loss is approximately 10 dB, with the majority of this loss attributed to the taper and grating couplers (details in the Supplementary Information).

The responsivity, defined as $\mathcal{R} = I_{ph}/P_{in}$, where I_{ph} is the photocurrent in amperes and P_{in} is the waveguide-coupled optical power in watts incident on the GWG-PD, is measured as a function of input optical power with an excitation wavelength of 1550 nm and applying a voltage bias of -9 V across electrodes (Fig. 2b). We observed a decrease in responsivity from 0.56 A/W to 0.13 A/W at higher input optical power. This reduction may be attributed to several interconnected factors: i) as optical power increases, the photodetector may reach saturation, resulting in a nonlinear relationship between photocurrent and incident light intensity; ii) higher carrier densities can enhance recombination processes, especially through non-radiative pathways, which reduces the overall photocurrent; iii) increased thermal effects from higher optical power can alter the material properties, leading to changes in dark current and bandgap energy, and iv) Auger effects can lead to an increase in carrier density that enhances recombination processes, ultimately decreasing the responsivity.

We found that the responsivity at 1550 nm under an input optical power of 125 nW incident on the GWG-PDs increases from 0.12 A/W to 0.56 A/W as the reverse bias voltage increases (Fig. 2c). This increase is primarily due to the higher electric field in the Te-implanted Si region, which accelerates the separation and collection of photogenerated carriers. The stronger field enhances the drift velocity of electrons and holes, reducing recombination losses and thereby boosting both photocurrent and responsivity. Additionally, a higher reverse bias expands the depletion region, allowing more incident light to be absorbed where carriers are swiftly collected, further enhancing efficiency. In contrast, at zero bias, responsivity is three orders of magnitude lower because carrier separation depends solely on the slower

diffusion process without an assisting electric field, leading to higher carrier recombination rates and thus lower responsivity.

We calculate the quantum efficiency (η) of the photodetectors at 1550 nm under a reverse bias of -9 V as $\eta(\lambda) = (\mathcal{R}_\lambda hc) \, / \, \lambda e$, where λ is the wavelength (nm), $\mathcal{R}_\lambda$ is photodetector responsivity (A/W) at a particular wavelength (λ), h is the Planck constant, c is the light speed in vacuum, and e is the elementary charge. The quantum efficiency was found to be η=44.8%.

To investigate the detection mechanism of the GWG-PDs and their wavelength-dependent responsivity, we fabricated lateral p-i-n photodetectors on an SOI chip, replicating the doping levels, implanted area dimensions, and annealing parameters of the GWG-PDs. The basic lateral p-i-n structure was repeated to create a large-area (3 mm^2) interdigitated photodetector, similar to that reported in Ref.[19]. The intrinsic region between the p- and n-doped layers of these devices was implanted with Te, P, and Si ions, respectively; followed by rapid thermal annealing to activate the dopants and repair implantation-induced damage.

The interdigitated Te-implanted Si photodetector demonstrates a unique dual-band responsivity, covering both visible-near infrared and telecom wavelength ranges (Fig. 2d). In the visible to near-infrared range, responsivity is achieved through Si bandgap absorption. In contrast, this large-area detector (3 mm^2), featuring a 140-nm-thick Te-implanted absorbing layer, exhibits a nearly flat responsivity in the telecom wavelength range (1260–1625 nm), including at 1550 nm, with a measured responsivity of approximately 0.01 A/W under a reverse bias of –4 V (Fig. 2d).

Typically, two distinct absorption bands would be expected in the responsivity spectrum, corresponding to the Te-induced double defect levels at E_c – 0.19 eV and E_c – 0.41 eV[16] within the Si bandgap. However, under a reverse bias of –4 V, these Te defect levels become ionized due to the strong electric field in the fully depleted intrinsic region (see Fig. 3b). This ionization process enables efficient absorption of sub-bandgap photons across the entire telecom wavelength range, resulting in the observed flat responsivity. In contrast, control devices implanted with P or Si lack responsivity in the telecom range, as the absorption coefficient of P- and Si defect-related intragap states at telecom wavelengths is several orders of magnitude lower than that of Te[20]. This limits their detection to photons with energies below the Si bandgap.

The dual-band behavior of the interdigitated Te-implanted detector enables responsivity across both visible-near infrared and telecom wavelengths, enhancing its versatility for broadband optical

applications. The Te-related intragap defects act as absorbing centers that do not generate thermally active carriers, allowing for exclusive sub-bandgap photon absorption within the Te-implanted region. This performance marks a record-high responsivity of 0.01 A/W for large-area extrinsic Si photodetectors in the telecom-wavelength range, demonstrating the unique potential of Te intragap states for short-wavelength infrared applications.
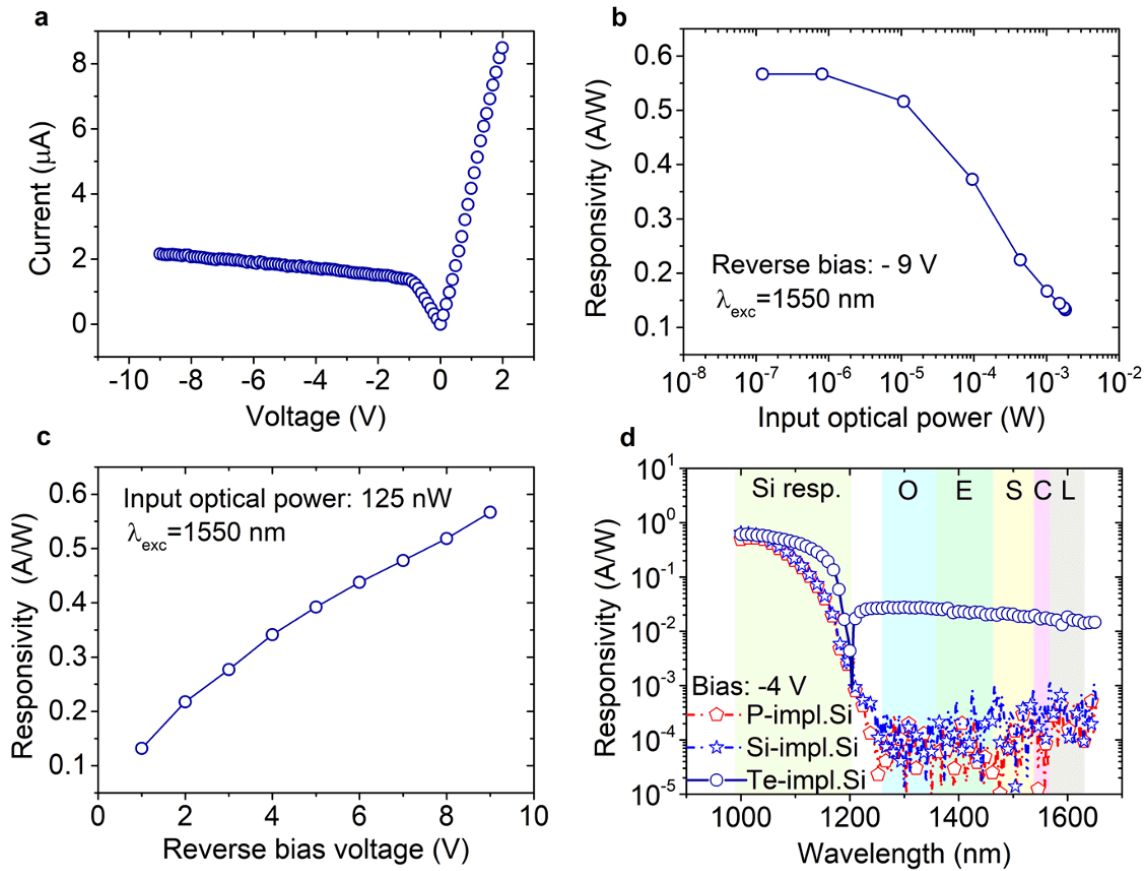
Figure 2. Room–temperature performance characteristic of an all–silicon GWG–PD with a Si:Te absorption length of L=300 μm. a, Dark current-voltage (I-V) characteristic under forward and reverse bias. **b,** Responsivity of the GWG–PD biased at –9 V as a function of input optical power at a wavelength of 1550 nm. **c,** Responsivity at 1550 nm for an input optical power of 125 nW, plotted against reverse bias voltage. **d,** Wavelength dependence of control devices, each reversely biased at –4 V, including large–area and top–illuminated Si-implanted Si, P-implanted Si, and Te-implanted Si p–i–n photodetectors, processed under the same conditions as the GWG–PD (i.e. dopant concentration and annealing). A nearly flat and high response is observed across all optical telecommunication bands for the large–area Te–implanted Si p–i–n photodetector. The responsivity values in **c** and **d** include an overall optical loss (i.e. both coupling and propagation losses) of 10 dB, determined from over 20 grating–waveguide–grating control structures with identical dimensions to the GWG–PDs.

Next, we characterized the GWG–PDs for NEP, which is the minimum incident optical power that a photodetector can distinguish from noise, indicating its sensitivity. Details are described in the Methods.

In Fig. 3a, we present the NEP at 1550 nm measured under a reverse bias of –4 V, which was found to be 4.2×10^{-10} W/(Hz)$^{1/2}$. This value is two orders of magnitude higher than commercial Ge photodetectors[21]. Despite the higher NEP, Te-implanted Si detectors offer key advantages for silicon photonic circuits, particularly in telecom-band applications, where reduced fabrication complexity and cost, integration, and scalability are prioritized over ultra-low NEP. A potential strategy to lower the NEP in the Te-implanted GWG–PDs involves optimizing the doping concentration and thickness of the Te-implanted layer to enhance sub-bandgap absorption efficiency while minimizing dark current.

The linear dynamic range (LDR), defined as LDR (dB) $= 10 \times \log_{10}(\mathrm{P_{max}}/\mathrm{P_{min}})$, represents the range of input optical power levels in watts, from the minimum ($\mathrm{P_{min}}$) to the maximum ($\mathrm{P_{max}}$), over which the detector exhibits a linear response to incident light. In this work, the (LDR) was found to be 33.7 dB for optical power levels ranging from 4.2×10^{-10} to 1×10^{-6} W, demonstrating the detector's capability to detect a wide range of optical power levels while maintaining linearity in its response.

We determined the bandwidth ($f_{BW} = 1/2\pi R_L C_j$) and the rise time response ($t_r = 0.35/f_{BW}$) of the GWG–PDs using the measured junction capacitance ($C_j = 5.4 \times 10^{-13}$F) obtained from the C-V characteristic (Fig. 3b) and the load resistance ($R_L = 50\Omega$). The calculated bandwidth is approximately 5.9 GHz, and the corresponding rise time response is estimated to be 59 ps. These results reflect the performance limit set by the junction capacitance and load resistance, emphasizing the photodetector's potential for high-speed operation in appropriately designed circuits.

The GWG–PDs with longer optical absorption lengths maintain similar responsivity at 1550 nm, yet they exhibit an order of magnitude higher NEP and slightly increased capacitance (details in the Supplementary Information). The consistent responsivity across varying device lengths (L) suggests that the 1550 nm laser light is fully absorbed within a 300 μm path, indicating effective optical absorption over this distance.
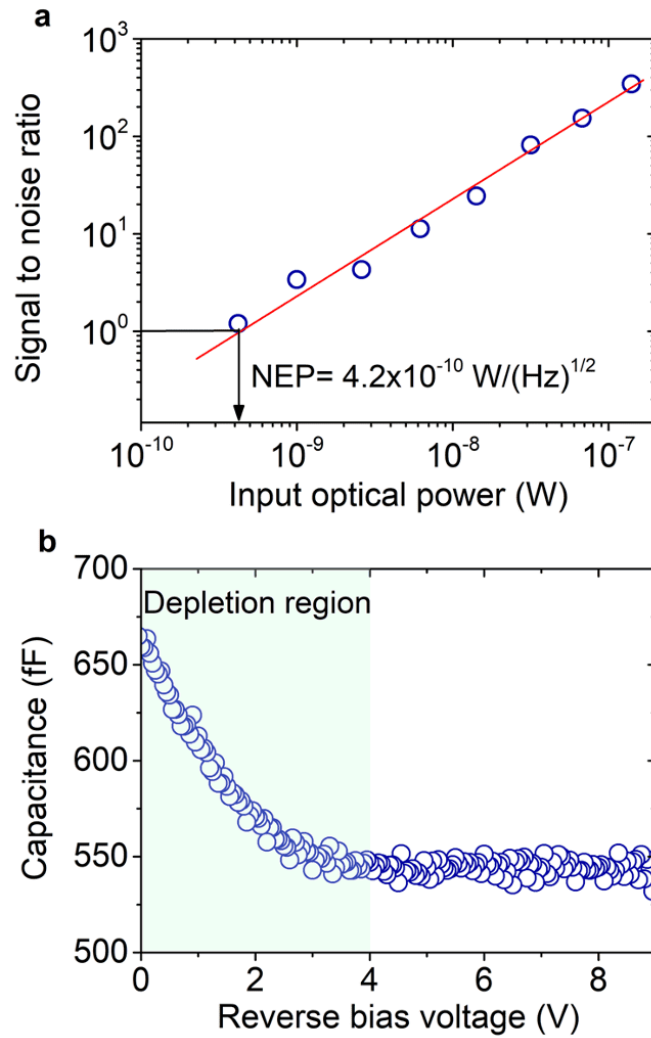
a, Plot showing Signal to noise ratio versus Input optical power (W). The data points follow a red trend line, with NEP= 4.2x10^{-10} W/(Hz)$^{1/2}$ marked at SNR = 1.

b, Plot showing Capacitance (fF) versus Reverse bias voltage (V), with a shaded "Depletion region" from 0 to 4 V.

Figure 3. Sensitivity, linear dynamic range, and capacitance of an all-silicon GWG-PD. a, Signal–to–noise ratio (SNR) derived from frequency-dependent current measurements as a function of input optical power at 1550 nm for the GWG-PD biased at –4 V, used to accurately determine the noise-equivalent power. **b,** Capacitance of the GWG-PD's p–i–n junction as a function of the reverse bias voltage.The intrinsic region is fully depleted at a reverse bias above 4 V.

Discussion

Next, we discuss the unique performance attributes of Te-implanted Si p-i-n photodetectors at equilibrium Te concentrations, particularly in grating- and waveguide-coupled designs, positioning them as a promising route for very-large-scale integration (VLSI) into PICs through monolithic fabrication. These Te-implanted Si devices benefit from using deep-level impurities in concentrations close to the solid solubility limit, which prevents thermally generated free carriers, allowing only sub-bandgap photon absorption. This behavior distinguishes our Te-implanted Si from hyperdoped Si, in which impurity concentrations often exceed the solubility threshold, resulting in heavy n-type doping and metallic-like behavior that degrade device performance by increasing leakage currents and noise, despite higher infrared absorption.

Waveguide-coupled detectors exhibit substantial advantages over traditional vertical detector designs by enabling extended optical absorption lengths along the rib waveguide structure, reaching hundreds of microns, thus significantly improving responsivity. When implemented on SOI substrates, these devices achieve substantial noise reduction, as the photodetectors are isolated from the bulk Si, eliminating noise-inducing interactions and enhancing signal integrity. Additionally, waveguide-coupled Te-implanted Si detectors can be fabricated with compact footprints, lowering their capacitance and enhancing speed, which is a critical advantage for achieving high bandwidths and fast response times.

Recently, double microring resonators (d-MRRs) were demonstrated as an effective solution to address the issue of crosstalk in wavelength-division multiplexing systems[22] by significantly reducing spectral tails around resonances, a limitation observed in single-MRR designs. Their ability to suppress crosstalk while maintaining high channel capacity makes them an ideal choice for integration with Te-implanted Si photodetectors. The combination of d-MRRs and Te-implanted Si enables enhanced absorption and responsivity, leveraging the material's high absorption coefficient and the resonant enhancement of the MRRs.

We anticipate that GWG Te-implanted Si photodiodes can be engineered to operate in avalanche mode, similar to avalanche photodiodes (APDs). This design, when integrated with d-MRRs, offers a pathway to further improve absorption and responsivity. Consequently, such APDs could achieve sufficient responsivity at relatively low gain levels, enabling them to exceed the bandwidth limitations of conventional high-speed receivers.

Methods

Fabrication

SOI substrates with a 220 nm silicon layer and a 2000 nm buried SiO_2 layer were utilized to fabricate on-chip grating- and waveguide-coupled silicon p-i-n photodetectors using electron beam lithography (EBL) and inductively coupled plasma reactive ion etching (ICP-RIE). The fabrication process included cleaning the substrates, applying a negative tone resist (hydrogen silsesquioxane), and exposing the patterns via EBL. After development, the patterns were transferred into the silicon layer through ICP-RIE. To form a p-i-n junction for efficient extraction of photogenerated electron-hole pairs, phosphorus and boron dopants were implanted to create n- and p-type regions, respectively. These regions were then subjected to annealing to activate the dopants and repair the implantation-induced defects. Additionally, tellurium ions were locally implanted to enable sub-bandgap absorption in silicon, with a rapid thermal annealing process conducted to repair implantation-induced defects and activate the Te dopants.

Electrical measurement

The current-voltage and capacitance-voltage characteristics were measured in the dark using a semiconductor device parameter analyzer (Agilent B1500A).

Responsivity measurement

The responsivity of the GWG-PD was measured at a wavelength of 1550 nm. A variable optical attenuator (V1550A) and signal generator (DGS3136B) were used to amplitude-modulate the input laser at 70 Hz. The modulated light was split, with one portion directed to a power meter (PM100USB) for real-time monitoring of incident power and the other directed to the GWG-PD's grating coupler. The light was coupled into the device at a 10° incidence angle using a cleaved single-mode fiber (SMF-28) after polarization adjustment via a manual polarization controller (FPC651). A trans-impedance amplifier (DLPCA-200) supplied bias to the device and amplified the photocurrent generated by the GWG-PD. The amplified signal was subsequently directed to a lock-in amplifier (SRS830), synchronized to the modulation frequency, for precise detection. Output data from the lock-in amplifier was collected and analyzed on a computer. A sketch of the measurement setup is provided in the Supplementary Information.

The spectral responsivity of the interdigitated Te-implanted silicon photodetector was measured using a different setup involving a Horiba Triax 550 monochromator in combination with a Quartz Tungsten Halogen (QTH) lamp. A set of collimator lenses was employed to couple the monochromator's output to a broadband multimode optical fiber, enabling measurements across a broad wavelength range of 400 to 2200 nm. The light output from the fiber was focused into the detector using an objective lens.

A chopper was used to modulate the light impinging on the photodetectors after it passed through a series of optical long-pass filters, which eliminated second-order optical contributions from the grating. The photocurrent generated by the photodetector was then coupled to a low-noise current preamplifier (DLPCA-200) and subsequently to a lock-in amplifier (SRS830) for signal acquisition. Finally, a calibrated pyroelectric detector (Newport DET-L-PYK5-R-P) was utilized to assess the optical response of the entire system.

Noise equivalent power and linear dynamic range measurement

To accurately determine the NEP and the linear dynamic range of the devices, we measured the device noise spectrum in the frequency domain using a low-noise current preamplifier connected to a spectrum analyzer. A 1550 nm laser, modulated with a 70 Hz square wave, was employed along with a set of neutral density filters to adjust the light intensity incident on the devices, ranging from picowatts to milliwatts.

We obtained the NEP by measuring the photodetector current spectral density under the modulated 1550 nm laser across different light intensities, using a measurement bandwidth of 1 Hz. The signal-to-noise ratio (SNR) was then plotted on a double logarithmic scale as a function of the input optical power at 1550 nm. The linear fit of the SNR derived from the frequency-dependent noise current reaches 1, indicating that the signal intensity matches the noise floor as defined by the NEP. This analysis also allows us to determine the linear dynamic range of the detector.

Statements and Declarations

Data availability

The data that support the plots within this paper and other findings of this study are available from the corresponding authors upon request.

Author Contributions

M.S.S. and Y.B. conceived the idea. M.S.S., M.T.C., A.E., R.L., Y.M.G., K.J., and Y.B. designed the device. M.T.C. conducted the simulations under the supervision of K.J. M.S.S., M.C.T., A.E., and R.L. fabricated the devices under the supervision of Y.M.G. M.S.S., S.P., S.Z., and Y.B. designed the implantation and annealing experiments. M.S.S., M.T.C., S.W., and Y.B. developed the characterization setup. M.S.S., M.T.C., S.W., and G.G.P. performed the characterization experiments and analyzed the data under the supervision of Y.B. All authors contributed to the discussion of the experimental results. M.S.S. and Y.B. wrote the manuscript with input from all co-authors. M.H., Y.M.G., K.J., S.Z., and Y.B. supervised and coordinated the entire project.

Conflicts of interests

The authors declare no competing interests.

References

1. [a], [b], [c]*Shekhar S, et al. Roadmapping the next generation of silicon photonics. Nat Commun. 15: 751 (2024).*

2. [a], [b]*Lischke S, et al. Ultra-fast germanium photodiode with 3-dB bandwidth of 265 GHz. Nat Photonics. 15: 925–931 (2021).*

3. [^]*Assefa S, Xia F, Vlasov YA. Reinventing germanium avalanche photodetector for nanophotonic on-chip optical interconnects. Nature. 464: 80–84 (2010).*

4. [^]*Huerta EA, et al. Convergence of artificial intelligence and high performance computing on NSF-supported cyberinfrastructure. J Big Data. 7: 88 (2020).*

5. [^]*Shastri BJ, et al. Photonics for artificial intelligence and neuromorphic computing. Nat Photonics. 15: 102–114 (2021).*

6. [^]*Savage N. Photodetectors. Nat Photonics. 1: 730–731 (2007).*

7. ᐞSun C, et al. Single-chip microprocessor that communicates directly using light. Nature. 528: 534–538 (2015).

8. ᐞBerencen Y, et al. Room-temperature short-wavelength infrared Si photodetector. Sci Rep. 7: 43688 (2017).

9. ᐞYou J-B, Kwon H, Kim J, Park H-H, Yu K. Photon-assisted tunneling for sub-bandgap light detection in silicon PN-doped waveguides. Opt Express. 25: 4284–4297 (2017).

10. ᐞWu L, et al. Bulk Defect-Mediated Absorption Sub-Bandgap All-Silicon Photodetector with Low Dark Current Density at Ambient Temperatures. ACS Photonics. 10: 3674–3681 (2023).

11. ᐞPeng Y, et al. All-silicon microring avalanche photodiodes with a >65 A/W response. Opt Lett. 48: 1315–1318 (2023).

12. a, b, cSher M-J, et al. Picosecond carrier recombination dynamics in chalcogen-hyperdoped silicon. Appl Phys Lett. 105: 053905 (2014).

13. ᐞRahman KA, et al. Temperature-Dependent Dynamics of Charge Carriers in Tellurium Hyperdoped Silicon. Adv Electron Mater. 2400417 (2024) doi:10.1002/aelm.202400417.

14. ᐞWang M, et al. Breaking the Doping Limit in Silicon by Deep Impurities. Phys Rev Appl. 11: 054039 (2019).

15. ᐞMailoa JP, et al. Room-temperature sub-band gap optoelectronic response of hyperdoped silicon. Nat Commun. 5: 3011 (2014).

16. a, bWang M, et al. Extended Infrared Photoresponse in Te-Hyperdoped Si at Room Temperature. Phys Rev Appl. 10: 024054 (2018).

17. ᐞSheehy MA. Femtosecond-laser microstructuring of silicon: dopants and defects. (Harvard University, 2004).

18. ᐞTaflove A, Hagness SC. Computational Electrodynamics. (Artech House, 2005).

19. ᐞShaikh MS, et al. On-chip lateral Si:Te PIN photodiodes for room-temperature detection in the telecom optical wavelength bands. Opt Express. 31: 26451–26462 (2023).

20. ᐞFan HY, Ramdas AK. Infrared Absorption and Photoconductivity in Irradiated Silicon. J Appl Phys. 30: 1127–1134 (1959).

21. ᐞVivien L, Pavesi L. Handbook of Silicon Photonics. Vol. Ch. 10. CRC Press; 2013.

22. ᐞPeng Y, et al. An 8 × 160 Gb s−1 all-silicon avalanche photodiode chip. Nat Photonics. 18: 928–934 (2024).

Declarations

Potential competing interests: No potential competing interests to declare.